Inorganic Chemistry

pubs.acs.org/IC Article

3-D Antimonotungstate Framework Based on 2,6-H_2pdca-connecting Iron−Cerium Heterometallic Krebs-type Polyoxotungstates for Detecting Small Biomolecules

Baoxing Zeng, Yan Zhang, Yanhong Chen, Guoping Liu, Yanzhou Li,* Lijuan Chen,* and Junwei Zhao*

Cite This: *Inorg. Chem.* 2021, 60, 2663−2671 Read Online

ACCESS | Metrics & More | Article Recommendations | Supporting Information

ABSTRACT: An inorganic−organic hybrid 3-D Fe^{III}−Ce^{III} heterometallic antimonotungstate framework $[Ce(H_2O)_5(2,6\text{-pdca})]_4H_2[Fe_4(H_2O)_6(SbW_9O_{33})_2]\cdot 38H_2O$ (**1**) (2,6-H_2pdca = 2,6-pyridine-dicarboxylic acid) has been synthesized via a hydrothermal method by the one-pot reaction of 2,6-H_2pdca, $FeCl_3\cdot 6H_2O$, $Ce(NO_3)_3\cdot 6H_2O$, and $Na_9[B\text{-}\alpha\text{-}SbW_9O_{33}]\cdot 19.5H_2O$. Notably, the structural unit of **1** possesses a Krebs-type $[Fe_4(H_2O)_6(2,6\text{-pdca})_2(SbW_9O_{33})_2]^{10-}$ subunit supported with four bridging $[Ce(H_2O)_5(2,6\text{-pdca})]^+$ moieties. It is worth highlighting that adjacent structural units are concatenated together through heterobimetallic bridges to construct a 3-D framework. Furthermore, cuboid nanocrystal **1′** was prepared under mild hydrothermal conditions based on the electrostatic interaction between **1** and K^+. The effects of concentration and time on the morphology of nanocrystal **1′** were also studied. The cuboid nanocrystal **1′** was used as a modified electrode material for simultaneous electrochemical detection of dopamine and acetaminophen. The **1′**-modified glassy carbon electrode shows good selectivity and sensitivity for detecting dopamine and acetaminophen.

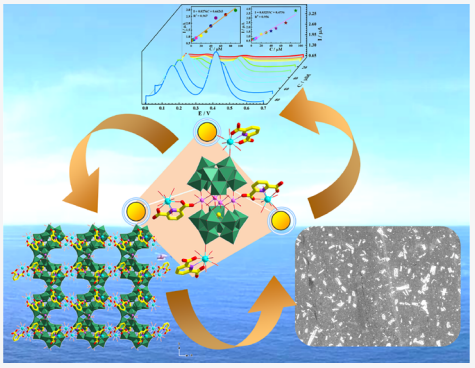

INTRODUCTION

Polyoxotungstates (POTs), as nanosized metal-oxide clusters, are formed by numerous $\{WO_x\}$ (x = 4−7) polyhedra with various linked modes, such as sharing corners, edges, or faces, which vary in their shapes, sizes, constructions, and stacking modes, ranging from discrete clusters to 3-D extend frameworks.[1,2] Changing the complicated components of POTs enables us to obtain their tunable structures with excellent properties, such as for electrochemistry, catalysis, magnetism, sensors, energy, luminescence, and so forth.[3−9] Lacunary POTs with diversiform vacant sites have drawn great attention in the past years due to their strong capability of coordination toward transition metals (TMs) or lanthanides (Lns), thereby resulting in functional metal-substituted POTs with spectacular architectures.[10−12] Therefore, the incorporation of bimetal species and organic ingredients to lacunary POT matrices can result in inorganic−organic hybrid TM−Ln heterometallic architectures of significant novelty.[13] In addition, the delicately synergetic effects among heterometallic metal types, POT entities, and organic components can create extraordinary phenomena.[14] Therefore, some TM−Ln heterometallic inorganic−organic hybrid POT (TMLnHIOHPOT) species have been reported, as indicated in the review reported by our group.[15] Nonetheless, there are even fewer reports about TM−Ln heterometallic inorganic−organic hybrid antimonotungstates (TMLnHIOHATs) in TMLnHIOHPOTs.[16,17] For example, Reinoso and partners constructed a group of tetrameric TMLnHIOHATs $[Sb_7W_{36}O_{133}Ln_3TM_2(OAc)(H_2O)_8]^{17-}$ (TM = Co^{2+}, Ln = Gd^{3+}, La^{3+}; TM = Ni^{2+}, Zn^{2+}; Ln = Ce^{3+}) with a $\{MW_9O_{33}\}$ capping unit.[16] Kong et al. successfully prepared three $\{Sb_4O_4\}$-bridging tetrameric TMLnHIOHATs $[Ln_3(H_2O)_5Ni(H_2O)_3(Sb_4O_4)(B\text{-}\alpha\text{-}SbW_9O_{33})_3(NiW_6O_{24})(WO_2)_3(CH_3COO)]^{17-}$ (Ln = Nd^{3+}, Pr^{3+}, La^{3+}) based on the anionic template method.[17] The scarcity of reports about TMLnHIOHATs might probably be on account of synthetic obstacles such as competing reactivities between TM and Ln species leading to only-TM-included or only-Ln-included ATs.

In order to overcome the synthetic obstacles faced by the construction of TMLnHIOHATs, our group found that the introduction of carboxylic acid ligands can effectively obtain TMLnHIOHATs in the case of Fe^{3+} as the TM resource. For instance, early in 2014, our group reported a series of amino acid-functionalized FeLnHIOHATs $[Ln(H_2O)_8]_2[Fe_4(H_2O)_8(thr)_2][B\text{-}\beta\text{-}SbW_9O_{33}]^{2-}$ (thr = threonine; Ln = Lu^{3+}, Dy^{3+}, Gd^{3+}, Eu^{3+}, Sm^{3+}, Nd^{3+}, Pr^{3+}).[18] Four years later, *N*-heterocyclic aromatic carboxylic acid ligands with high steric

Received: December 4, 2020
Published: January 25, 2021

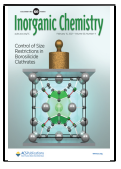

https://dx.doi.org/10.1021/acs.inorgchem.0c03556
Inorg. Chem. 2021, 60, 2663−2671

hindrance and less activity were introduced to construct FeLnHIOHATs. To our surprise, three types of 2-picolinic acid-decorated FeLnHIOHATs with zero-to-three dimensions were reported.[19] It is believed that the reasons for the successful acquisition of FeLnHIOHATs may be the following. (i) The strongly electrophilic Fe^{3+} ion can react effectively with nucleophilic lacunary AT precursors to produce the Fe^{3+}-substituted AT aggregates. (ii) Partial carboxylic groups of organic ligand prefer to coordinate with Fe^{3+} in the Fe^{3+}-substituted AT aggregates rather than Ln cations, which reduces the competition between Ln and Fe^{3+} ions to some extent. (iii) Furthermore, the oxytropism of Ln ions is more conductive to coordinate with AT building blocks. (iv) *N*-Heterocyclic aromatic carboxylic acid ligands with high steric hindrance also further induce the structural diversity of TMLnHIOHATs.

Inspired by above ideas, 2,6-pyridine-dicarboxylic acid (2,6-H_2pdc), which possesses relatively high coordination sites, a rigid "pyridine spacer", and versatile coordination behaviors, makes for integrating TM and/or Ln ions and even W atoms together in the formation of TMLnHIOHPOTs;[20] it was further introduced into our reaction system. A novel 2,6-H_2pdca-connecting Krebs-type $Fe^{III}Ce^{III}$HIOHAT $[Ce(H_2O)_5(2,6\text{-pdca})]_4H_2[Fe_4(H_2O)_6(SbW_9O_{33})_2]\cdot 38H_2O$ (**1**) was isolated based on a hydrothermal method (Figure 1)

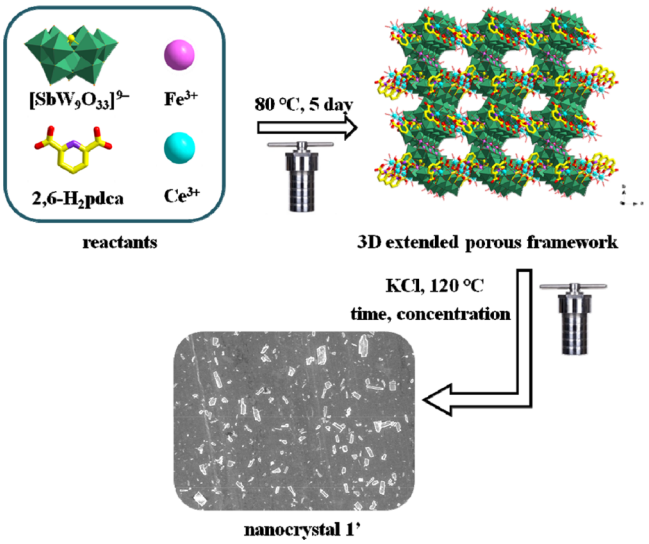

Figure 1. Synthetic route of **1** and nanocrystals of **1′**.

and was characterized by single-crystal X-ray diffraction, TG analysis, IR spectra, powder X-ray diffractions (PXRD), and elemental analyses (Table S1, Figures S1−S3). Interestingly, **1** displays a 3-D extended porous framework, which belongs to a six-connected topology with a Schläfli symbol of $(4^{12}\cdot 6^3)$. On the other hand, due to the tunable chemical and physical properties by controlling size, shape, and chemical composition of nanosized-POTs,[21−26] based on the electrostatic interaction between **1** and K^+, **1** was further prepared as nanocrystal **1′** with a uniform cuboid morphology when the reaction concentration was controlled. The basic skeleton structure retention of **1** in the nanocrystal **1′** was verified by IR spectra and PXRD analysis after **1** reacted with excess of K^+ countercation in the hydrothermal reactor. Inspired by the large specific surface area and more exposed active sites compared with the macroscopical crystals, nanocrystal **1′**-5 mL-2h as a modified electrode material presents a high electrochemical sensing capability and anti-interference performance toward detecting dopamine (DOP) and acetaminophen (AAP). The simultaneous detection of DOP and AAP with high sensitivity, low detection limit, and wide sensing concentration range in this work provides a typical prototype that shows that TMLnHIOHATs can be treated as modified electrode materials to detect two or more small biomolecules.

RESULTS AND DISCUSSION

Structure Description. Crystallographical data indicate that **1** crystallizes in the monoclinic space group $P2_1/c$ (Table S1). Bond valence sum (BVS) calculation results illustrate that chemical valences of Sb, W, Fe, and Ce centers in the polyoxoanion (POA) of **1** are +3, +6, +3, and +3 (Table S2). The tested PXRD pattern of **1** is in accord with the mimic XRD pattern, elucidating its good phase purity (Figure S2). Its molecular unit includes a Krebs-type Fe−Ce heterometallic POA $[Ce(H_2O)_5(2,6\text{-pdca})]_4[Fe_4(H_2O)_6([B\text{-}\beta\text{-}SbW_9O_{33})_2]^{2-}$ (**1a**) (Figure 2a, b), two H^+ protons, and thirty-eight lattice waters. **1a** consists of a $\{Fe_4\}$-encapsulated sandwich-type $[Fe_4(H_2O)_6(B\text{-}\beta\text{-}SbW_9O_{33})_2]^{6-}$ (**1b**) cluster (Figure 2a, b) and four $[Ce(H_2O)_5(2,6\text{-pdca})]^+$ groups (Figure 2c, d). Four $[Ce(H_2O)_5(2,6\text{-pdca})]^+$ groups in a parallelogram geometry (Ce···Ce: 11.728 × 15.032 Å) (Figure S4) are carried around the surface of the **1b** cluster, in which $[Ce1(H_2O)_5(2,6\text{-pdca})]^+$ groups connect with **1b** through the Ce1−O19−W7 bonds (150.1°) (Figure 2c), whereas $[Ce2(H_2O)_5(2,6\text{-pdca})]^+$ groups link to **1b** based on the C8−O41−Fe2 bonds (132.5°) (Figure 2d). The coordination spheres of Ce^{3+} centers in four $[Ce(H_2O)_5(2,6\text{-pdca})]^+$ groups can be divided into two types of nonacoordinate distorted bicapped triangular prism configurations. The $Ce1^{3+}$ coordination sphere is established by a N atom [Ce1−N1:2.643(10) Å] and two carboxyl oxygen atoms from the 2,6-$pdca^{2-}$ ligand [Ce1−O34:2.507(9) Å; Ce1−O36:2.510(8) Å], a μ_2-O atom from one $[B\text{-}\beta\text{-}SbW_9O_{33}]^{9-}$ subunit [Ce1−O19:2.572(9) Å], and five water ligands [Ce1−O4W: 2.526(11) Å; Ce1−O5W: 2.514(12) Å; Ce1−O6W: 2.510(9) Å; Ce1−O7W: 2.549(9) Å; Ce1−O8W: 2.530(9) Å] (Figure 2e, Table S3). The $Ce2^{3+}$ coordination sphere can also be determined by a N atom [Ce2−N2:2.641(11) Å] and two carboxyl oxygen atoms from one 2,6-$pdca^{2-}$ ligand [Ce2−O39:2.500(9) Å; Ce2−O40:2.537(8) Å], water ligands [Ce2−O9W: 2.533(11) Å; Ce2−O10W: 2.544(10) Å; Ce2−O11W: 2.532(10) Å; Ce2−O12W: 2.571(10) Å; Ce2−O13W: 2.511(11) Å], and a μ_2-O atom from the **1b** cluster [Ce2−O26:2.521(9) Å] (Figure 2f, Table S3). Within the **1b** cluster, four Fe^{3+} centers construct a parallelogram geometry with the Fe···Fe distance of 5.6 × 6.0 Å (Figure 2g, h and Figure S5). Both $Fe1^{3+}$ and $Fe2^{3+}$ centers exhibit an eight-coordinated hexahedral geometry (Figure 2i, j). Therein, the $Fe1^{3+}$ center is defined by three μ_2-O atoms from two $[B\text{-}\beta\text{-}SbW_9O_{33}]^{9-}$ subunits [Fe1−O17:1.942(8) Å; Fe1−O32:1.974(9) Å; Fe1−O22:1.957(9) Å], one carboxyl oxygen atom from the 2,6-$pdca^{2-}$ ligand [Fe1−O37:2.006(9) Å], and two aqua ligands [Fe1−O1W: 2.081(10) Å; Fe1−O2W: 2.103(8) Å] (Figure 2i). The $Fe2^{3+}$ center is determined by four μ_2-O atoms from two $[B\text{-}\beta\text{-}SbW_9O_{33}]^{9-}$ subunits [Fe2−O7:1.977(9) Å; Fe2−O21:1.957(8) Å; Fe2−O25:1.970(9) Å; Fe2−O33:1.956(9) Å], one carboxyl oxygen atom from the 2,6-$pdca^{2-}$ ligand [Fe2−O41:2.068(8) Å], and one aqua ligand [Fe2−O3W: 2.088(9) Å] (Figure 2j). In addition, it is considered that the $[B\text{-}\beta\text{-}SbW_9O_{33}]^{9-}$ subunit in

https://dx.doi.org/10.1021/acs.inorgchem.0c03556
Inorg. Chem. 2021, 60, 2663−2671

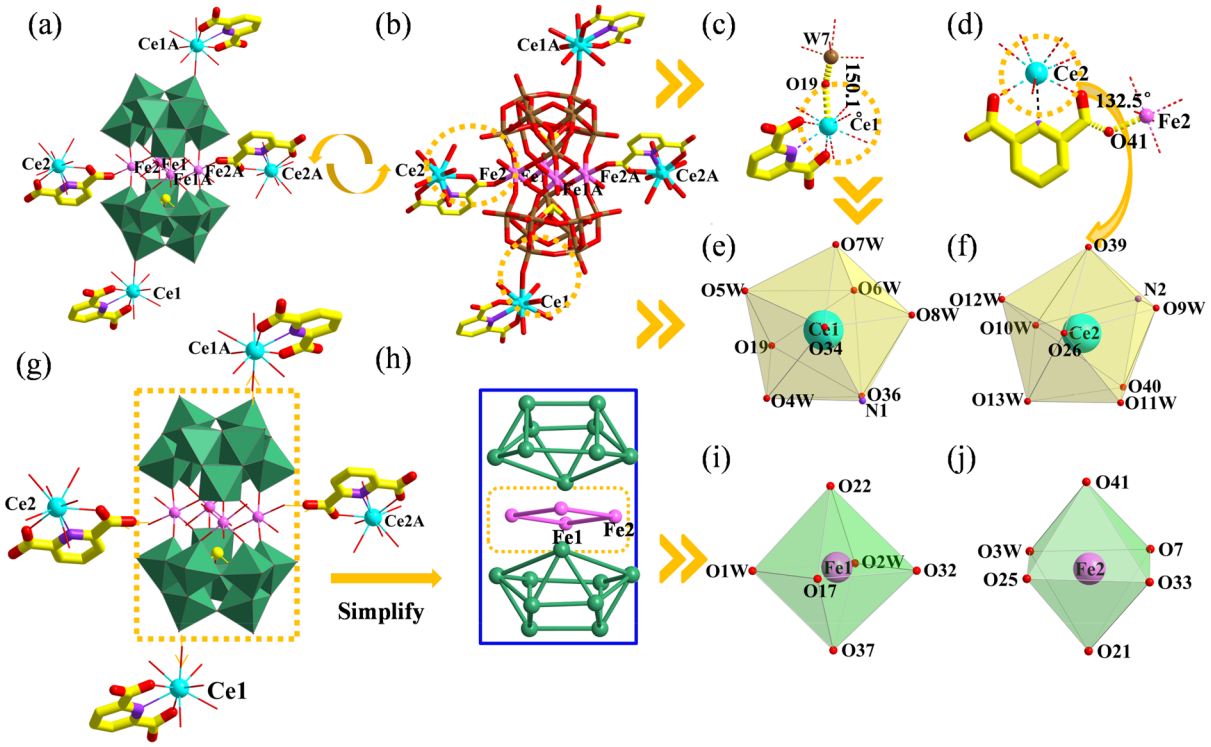

Figure 2. (a) Polyanionic structure of **1**. (b) Simplified view of **1**. (c) Structure of the $[Ce1(H_2O)_5(2,6\text{-pdca})]^+$ group. (d) Structure of the $[Ce2(H_2O)_5(2,6\text{-pdca})]^+$ group. (e, f) Contorted bicapped trigonal prismatic geometries of $Ce1^{3+}$ and $Ce2^{3+}$ cations. (g) Combination between the $[Fe_4(H_2O)_6(B\text{-}\beta\text{-}SbW_9O_{33})_2]^{6-}$ cluster and four $[Ce(H_2O)_5(2,6\text{-pdca})]^+$ groups in **1**. (h) Simplified view of $[Fe_4(H_2O)_6(B\text{-}\beta\text{-}SbW_9O_{33})_2]^{6-}$. (i, j) $Fe1^{3+}$ and $Fe2^{3+}$ ions showing octahedral coordination environments. Color codes: WO_6, sea green; Ce, turquoise; Sb, yellow; Fe, pink; O, red; C, gold; N, plum.

1b is derived from structural isomerization of the $[B\text{-}\alpha\text{-}SbW_9O_{33}]^{9-}$ fragment during the assembly process (Figure S6a, b), which might be caused by the low pH value of mixed solution.

What's more, viewed along the *bc* plane, the up−down neighboring units of **1** are connected to each other by the C7−O37−Fe1 bonds, giving birth to the "broken line" 1-D chains (Figure 3a). Meanwhile, these parallel broken line 1-D chains link with each other via the connection of $[Ce1(H_2O)_5(2,6\text{-pdca})]^+$ groups and $Fe1^{3+}$ ions of adjacent units, further forming a unique 2-D layer (Figure 3b). Think of [Ce1-(H2O)5(2,6-pdca)]$^+$ groups as linkers and **1b** as nodes, and the 2D layer can be further simplified as Figure 3c. Finally, the adjacent 2-D layers are interconnected by $Fe2^{3+}$ ions and $[Ce2(H_2O)_5(2,6\text{-pdca})]^+$ groups of adjacent units, which leads to a 3-D extended porous framework (Figure 3d). In other words, viewed along the *c* axis, four molecular units of **1** constitute an irregular 1-D pore (Figure 3e), and the successive 1-D pores resemble a 1-D pipeline in the 3-D framework. In addition, think of $[Ce(H_2O)_5(2,6\text{-pdca})]^+$ groups as the linkers; topologically, **1** displays a six-connected topology with a Schläfli symbol of $(4^{12}\cdot6^3)$ (Figure 3f). Therefore, 3-D packing of **1** illustrates that $[Ce(H_2O)_5(2,6\text{-pdca})]^+$ groups play a significant role in constructing its 3-D porous framework.

Preparation and Characterization of Nanocrystal 1′. With the help of electrostatic interaction between **1** and K^+, **1** rapidly precipitates as nanocrystal **1′** under hydrothermal conditions. To observe the morphology of **1′**, scanning electron microscopy (SEM) was employed by spreading the sample suspension onto the Si foil. As shown in Figure 4a, a large number of well-dispersed cuboid nanocrystals of **1′** were observed, and the sizes of nanocrystals of **1′** are in the range of 0.21−4.60 μm (Figure 4b, c). Moreover, dynamic light scattering (DLS) analysis results indicate that the average grain diameter of nanocrystal **1′** was about 0.249 μm. In addition, the stability of such nanocrystal solutions was also verified by DLS analysis, which shows good stability after one week (Figure S7). EDS image and EDS mapping images were performed to confirm the elemental compositions of **1′** (Figure 4d). The EDS mapping images certify that Sb, Ce, Fe, W, C, N, and O elements are homogeneously dispersed in the as-synthesized nanocrystals of **1′** (Figure 4e). In order to obtain nanocrystals of **1′** with better morphology, the concentration of **1** and K^+ and the reaction time were more tightly regulated. First, we investigated the effect of reactant concentration on the morphology of nanocrystals of **1′**. When the dosage of the deionized water is 2 mL, the morphology of nanocrystals of **1′** (named as **1′**-2 mL) is irregular (Figure S8a). As the dosage of deionized water increases to 5 mL, the uniform cuboid nanocrystals of **1′** (named as **1′**-5 mL) with good dispersion are observed (Figure S8b). With the deionized water continuously increasing to 10 mL, less uniform cuboid and plentiful spherical microcrystals of **1′** (named as **1′**-10 mL) appear (Figure S8c). Therefore, the reaction system with 5 mL water is the best condition for the synthesis of nanocrystal **1′** with good morphology. It was found that the concentration of reactants played an important role in the synthesis of nanocrystals of **1′**. The effect of reaction time on the morphology of nanocrystals of **1′** was also studied under the condition with 5 mL water (Figure S9). However, it was found that the reaction time showed negligible effect on the

https://dx.doi.org/10.1021/acs.inorgchem.0c03556
Inorg. Chem. 2021, 60, 2663−2671

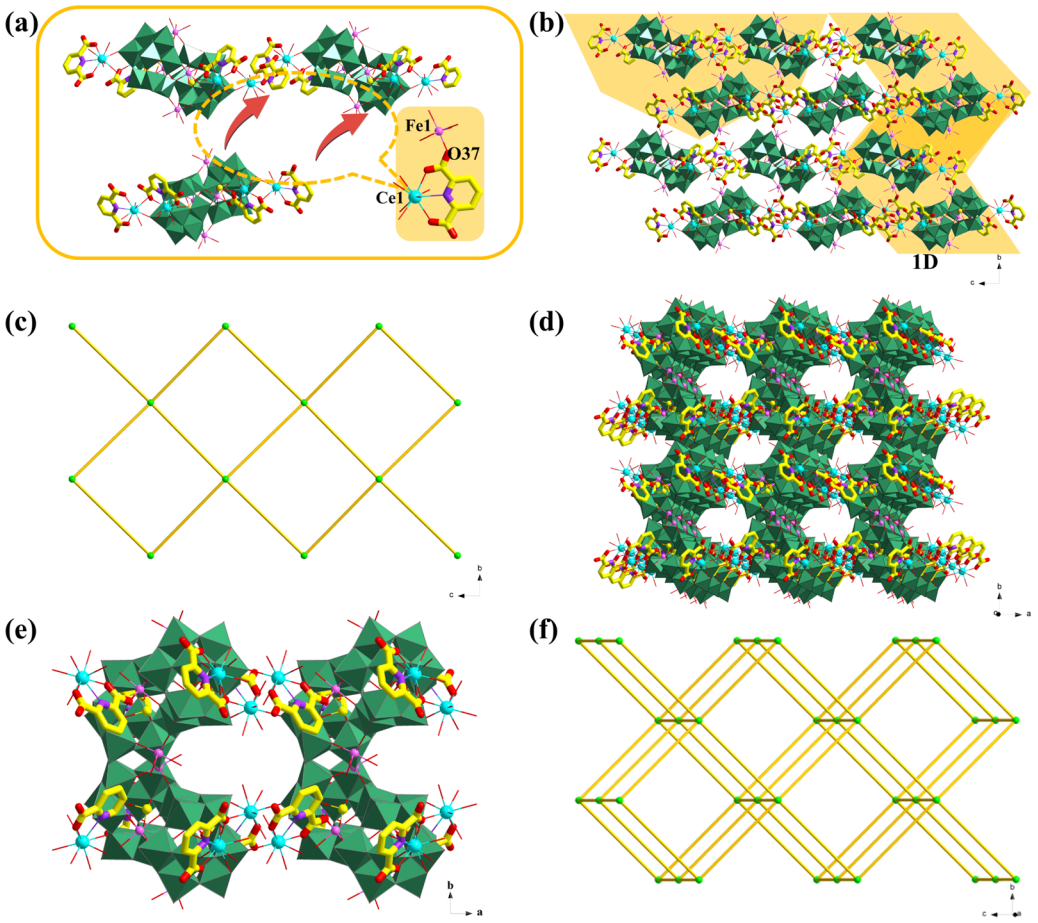

Figure 3. (a) 1-D chain structure of **1** (top) and its structural unit (bottom). (b) 2-D layer structure of **1**. (c) Simplified diagram of the 2-D layer structure. (d) 3-D extended porous framework. (e) 1-D pores along the *c* axis in **1**. (f) 3-D topological structure of **1**.

morphology of nanocrystal **1′** in this experiment. Furthermore, in order to prove the structure of nanocrystal **1′**, IR spectra and PXRDs of nanocrystal **1′** synthesized under varying reaction conditions were measured (Figure 5, Figure S10). Both their IR spectra and PXRDs are almost similar to the IR spectrum and PXRD of **1**, which apparently demonstrate that the structure of $[Ce(H_2O)_5(2,6\text{-pdca})]_4[Fe_4(H_2O)_6([B\text{-}\beta\text{-}SbW_9O_{33})_2]^{2-}$ is maintained in nanocrystals of **1′**.

Electrochemical Sensing Properties. DOP, as one of the crucial catecholamine neurotransmitters, exists in the nephritic, hormonal, central nervous system, as well as cardiovascular system and plays a significant role in mammalian central nervous system. The abnormal concentration of DOP in brain is generally related to neuropsychiatric disease.[27−29] Hence, sensitive and rapid determination of the concentration of DOP is extremely important. The normal concentration range of DOP for a healthy individual is approximately 10^{-7}−10^{-3} M.[30] AAP is a well-known pain-relieving and antipyretic medicine and is used extensively for relieving cold, fever, cough, and pain. Typically, a small dosage (below 0.03 g L^{-1}, about 0.20 M) of AAP is safe and does not show any serious side effect.[31] However, an overdose of AAP can lead to the accumulation of toxic metabolites, bringing about liver and kidney impairment.[32] Consequently, the accurate detection of AAP is also important for quality control of medicine and avoiding serious risks to human health. Therefore, it becomes very important to design electrochemical sensors that can simultaneously and effectively detect AAP and DOP in the body fluids. Thus, we try to use the nanocrystals of **1′** as the electrode materials to recognize them simultaneously.

First, the detecting measurements of modified electrodes by nanocrystal **1′** with different morphologies were studied. Compared with the CV method, the DPV method could obtain better sensitivity to detect small biomolecules because intensive signals could be gained by eliminating the non-Faradaic currents that occur with CV. Therefore, the DPV responsive curves for **1′**-modified GCEs toward DOP were performed by using **1′**-2 mL/GCE, **1′**-5 mL/GCE, and **1′**-10 mL/GCE in 0.10 M PBS in the presence of 0.50 mM DOP (Figure 6a), in which it is evident that an oxidation peak ascribed to DOP appears at $E_{1/2}$ = 0.136 V. Compared to **1**-modified GCE (named as **1**/GCE), the oxidation peak currents of DOP based on **1′**-*X* mL/GCEs (*X* = 2, 5, 10) show remarkable increase (Figure 6a, b). Furthermore, the oxidation peak current of **1′**-5 mL/GCE is the strongest (Figure 6b). These results indicate that nanocrystal **1′**-5 mL with high crystallinity and regular nanomorphology can exhibit better detection ability because of the more exposed active sites and long-range ordered structure. Also, we studied the influences of nanocrystals of **1′**-5 mL obtained at different reaction times on their electrochemical properties. The DPV responsive curves of **1**/GCE, **1′**-5 mL-2h/GCE, **1′**-5 mL-4h/GCE, **1′**-5 mL-8h/GCE, and **1′**-5 mL-12h/GCE were tested in 0.10 M PBS in the presence of 0.50 mM DOP (Figure 6c). Apparently, nanocrystals of **1′**-5 mL synthesized under different times exhibit a much better sensing ability than

https://dx.doi.org/10.1021/acs.inorgchem.0c03556
Inorg. Chem. 2021, 60, 2663−2671

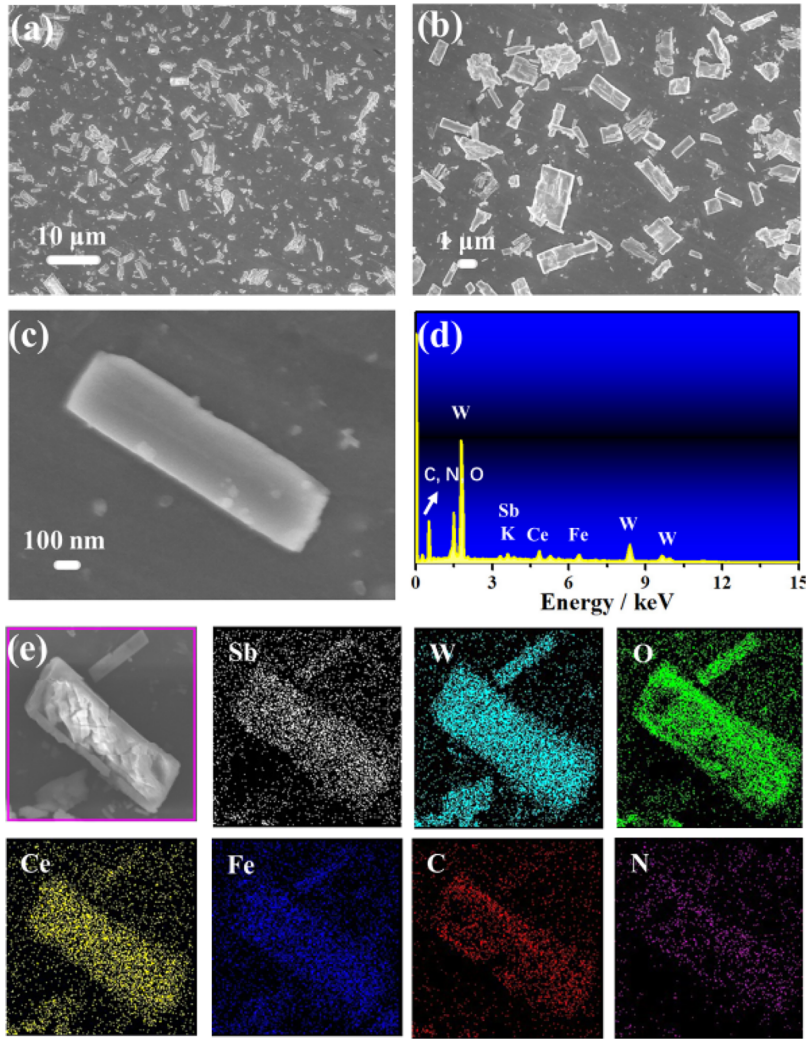

Figure 4. (a–c) SEM image of **1′**-5 mL with different magnifications. (d, e) EDS image and EDS mapping images of **1′**-5 mL with Sb, W, Ce, K, Fe, C, N, and O elements.

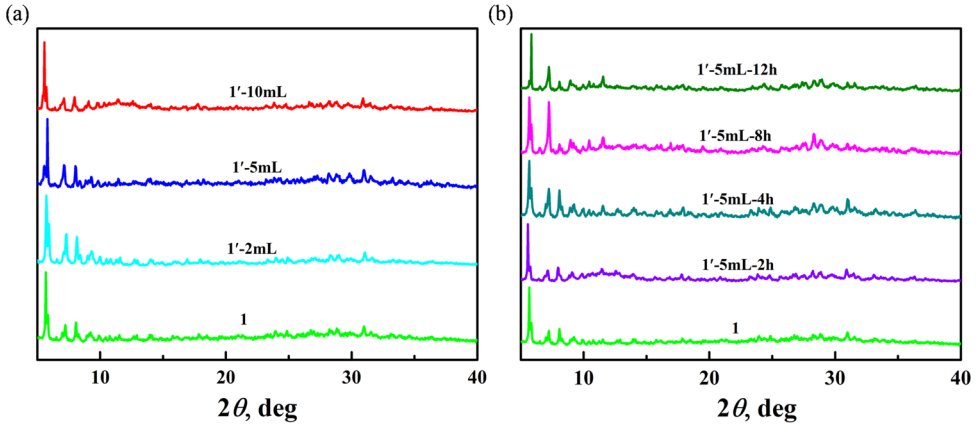

Figure 5. PXRD profiles of **1** and nanocrystal **1′** obtained by changing reaction time (a) and temperature (b).

single crystals of **1**. However, it should be noted that the sensing ability of **1′**-5 mL synthesized under different times basically have no discrepancy (Figure 6d), which further indicates that the sensing ability is dominated by the morphology of **1′** controlled by the concentration of **1** and K^+. Therefore, **1′**-5 mL-2h/GCE was chosen as the electrochemical sensor (ECS).

First of all, the stability of **1′**-5 mL-2h/GCE was tested before electrochemical detection. The CV measurements for **1′**-5 mL-2h/GCE ECS in 0.10 M PBS in the presence of 0.50 mM DOP and 0.50 mM AAP were carried out for 30 cycles. Results demonstrate that the CV shape and the peak currents of DOP and AAP do not show apparent variation after 30 cycles (Figure S11), manifesting the good stability and

https://dx.doi.org/10.1021/acs.inorgchem.0c03556
Inorg. Chem. 2021, 60, 2663–2671

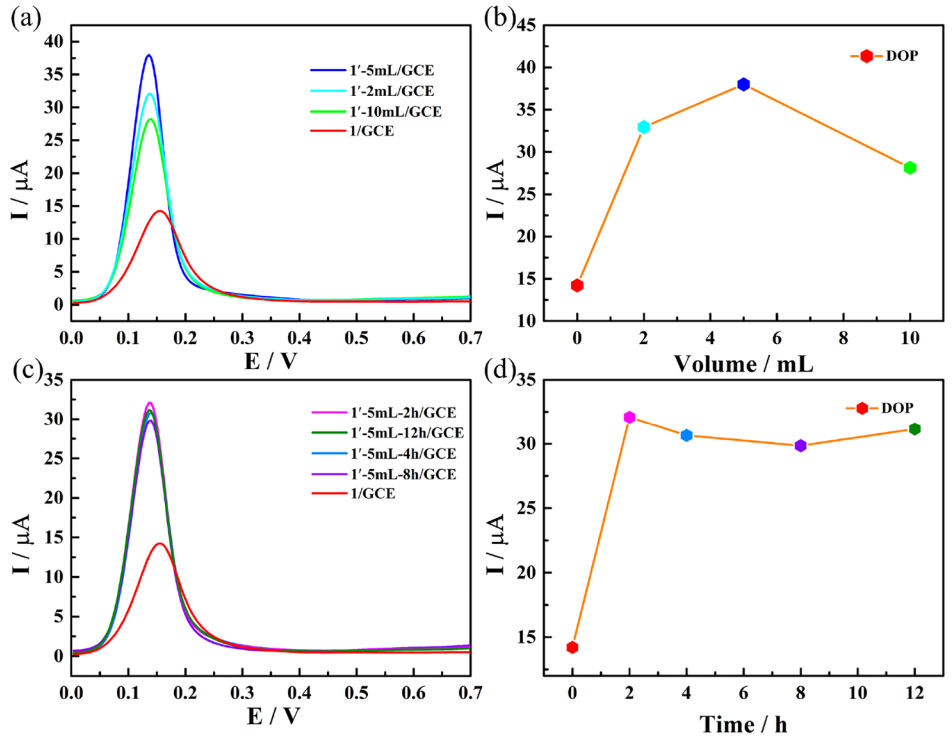

Figure 6. (a, b) Comparisons of DPV curves and DPV peak currents for **1**/GCE, **1**′-2 mL/GCE, **1**′-5 mL/GCE, and **1**′-10 mL/GCE toward 0.50 mM DOP. (c, d) Comparisons of DPV curves and DPV peak currents for **1**/GCE, **1**′-5 mL-2h/GCE, **1**′-5 mL-4h/GCE, **1**′-5 mL-8h/GCE, and **1**′-5 mL-12h/GCE toward 0.50 mM DOP.

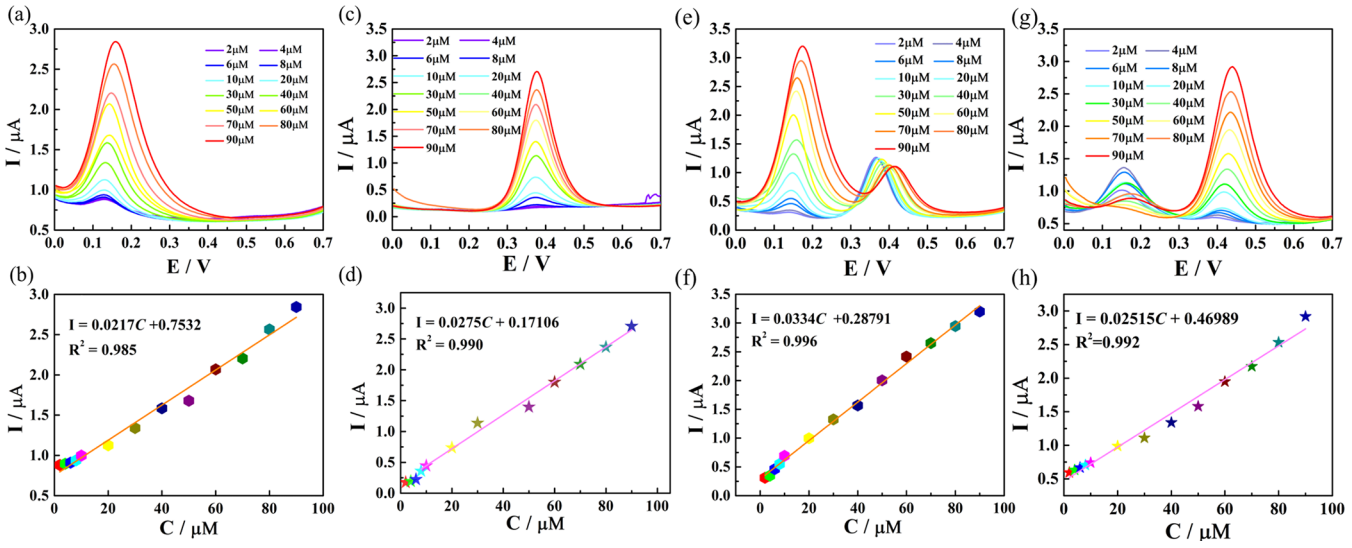

Figure 7. (a, b) Evolution of DPV curves and linear relation of DPV peak currents for **1**′-5 mL-2h/GCE ECS with increasing DOP concentration from 2 to 90 μM. (c, d) Evolution of DPV curves and linear relation of DPV peak currents for **1**′-5 mL-2h/GCE ECS with increasing APP concentration from 2 to 90 μM. (e, f) Evolution of DPV curves and linear relation of DPV peak currents for **1**′-5 mL-2h/GCE ECS toward DOP in 0.10 M PBS containing 30 μM APP with varying DOP concentration in 2−90 μM. (g, h) Evolution of DPV curves and linear relation of DPV peak currents for **1**′-5 mL-2h/GCE ECS toward APP in 0.10 M PBS containing 30 μM DOP with varying APP concentration in the range of 2−90 μM.

reliability of **1**′-5 mL-2h/GCE ECS. Additionally, in order to identify the role of the nanocrystals of **1**′ during the electrochemical detection, the CV measurements of the bare GCE in 0.10 M PBS in the presence of 0.50 mM DOP and 0.50 mM AAP under different times were made (Figure S12a). As shown in Figure S12a, the CV peak currents of DOP and AAP decay rapidly in 10 min until they disappear. Although the bare GCE has a high current signal in the beginning, it has poor stability, and the current signal declines quickly. In contrast, the CV measurements for **1**′-5 mL-2h/GCE in 0.10 M PBS in the presence of 0.50 mM DOP and 0.50 mM AAP under different times show good stability and repeatability (Figure S12b). This phenomenon illustrates that nanocrystal **1**′ plays a key role in the process of simultaneously detecting DOP and AAP. Figure 7a demonstrates DPV responsive curves for **1**′-5 mL-2h/GCE ECS in 0.10 M PBS (pH = 7.0) with the concentration change of DOP from 2 to 90 μM, and the DPV responsive peak potential of DOP is at 0.136 V. Apparently,

https://dx.doi.org/10.1021/acs.inorgchem.0c03556
Inorg. Chem. 2021, 60, 2663−2671

the responsive peak currents of 1′-5 mL-2h/GCE ECS toward DOP gradually rise with increasing concentration of DOP (Figure 7a), which demonstrates that 1′-5 mL-2h/GCE ECS displays a good sensing performance toward DOP. As depicted in Figure 7b, the DPV responsive peak currents of DOP are linear with the DOP concentrations, which conforms to the linear equation of I (μA) = 0.0217C (μM) + 0.7532 (R^2 = 0.985) within the concentration range of 2−90 μM. The limit of detection (LOD) for 1′-5 mL-2h/GCE ECS toward DOP is calculated as 0.210 μM. In the same way, the DPV responsive peak current for 1′-5 mL-2h/GCE ECS toward AAP with the change of the AAP concentration (2−90 μM) has also been recorded. A similar tendency can be observed, namely, the DPV responsive peak current for 1′-5 mL-2h/GCE ECS toward AAP rises with the enhancement of the AAP concentration (Figure 7c), in which the oxidation peak at 0.376 V is assigned to AAP. Moreover, the DPV responsive peak current for 1′-5 mL-2h/GCE ECS toward AAP is proportional to the AAP concentration in the range of 2−90 μM and can be fitted by the linear equation of I (μA) = 0.0275C (μM) + 0.17106 (R^2 = 0.990), affording the LOD of 0.165 μM (Figure 7d). It is extremely obvious that 1′-5 mL-2h/GCE ECS reveals a wider linear range and a lower LOD for DOP and AAP in 0.1 M PBS solution. In addition, the DPV responsive peak potentials of DOP and AAP are respectively located at 0.136 and 0.376 V. The separation of their responsive peak potentials is 0.240 V, which provides enough precondition for simultaneously detecting them. Overall, 1′-5 mL-2h might be used as an ECS material to simultaneously detect DOP and AAP.

Thus, DPV responsive curves for 1′-5 mL-2h/GCE ECS toward the mixture of DOP and AAP were also measured. When the AAP concentration remains unchanged at 30 μM, the DPV responsive oxidation peak current for 1′-5 mL-2h/GCE ECS toward DOP increases linearly with its concentration in the range of 2−90 μM, which can be fitted by the equation I (μA) = 0.0334C (μM) + 0.28791 (R^2 = 0.996) (Figure 7e, f), while the DPV responsive oxidation peak current toward AAP changes slightly. Furthermore, simultaneous detection of DOP and AAP was also performed. DPV curves for 1′-5 mL-2h/GCE ECS were recorded in 0.10 M PBS (pH = 7.00) with simultaneously increasing concentrations of DOP and AAP from 2 to 90 μM (Figure 8a). Their corresponding DPV responsive peak currents for 1′-5 mL-2h/GCE ECS toward DOP and AAP gradually increase with simultaneously increasing the concentrations of DOP and AAP, which demonstrates that 1′-5 mL-2h/GCE ECS manifests good sensing performance toward DOP and AAP. As depicted in the insets of Figure 8a, the DPV responsive peak current for 1′-5 mL-2h/GCE ECS toward DOP is linear to the DOP concentration, satisfying with the linear function of I (μA) = 0.0276C (μM) + 0.66243 (R^2 = 0.967) within the concentration range between 2−90 μM, and the LOD is 0.165 μM. Meanwhile, the DPV responsive peak current for 1′-5 mL-2h/GCE ECS toward AAP is also linear to the concentration of AAP in the range from 2 to 90 μM with the linear function of I (μA) = 0.03255C (μM) + 0.4756 (R^2 = 0.956), and the LOD is 0.140 μM. It is clear that simultaneous determination of these two analytes using 1′-5 mL-2h/GCE as a sensor can be achieved with high sensitivity, lower LOD, and wider detection concentration range.

In addition, the effects of scan rate on peak currents of DOP and AAP for 1′-5 mL-2h/GCE ECS were also studied by CV

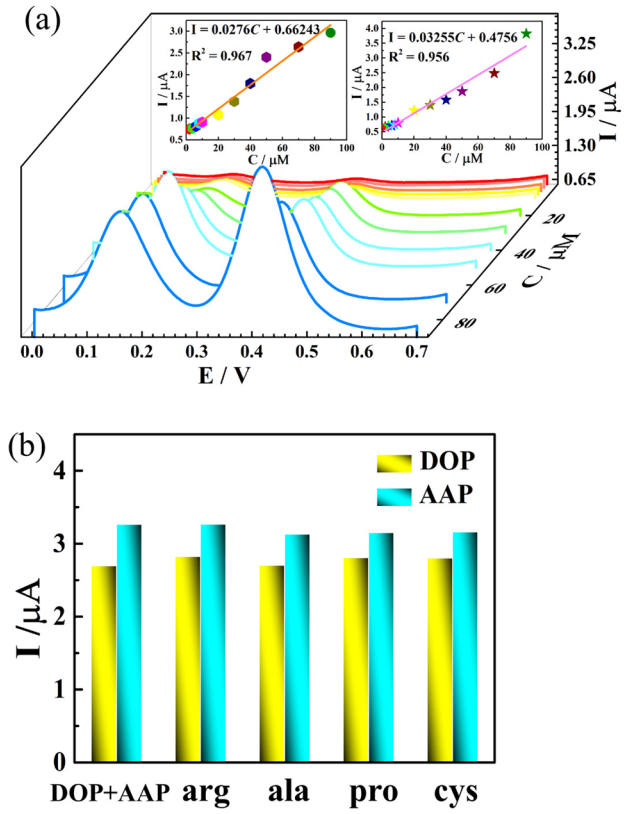

Figure 8. (a) The variation of DPV curves for 1′-5 mL-2h/GCE ECS in 0.10 M PBS (pH = 7.00) with simultaneously increasing concentrations of DOP and AAP from 2 to 90 μM. Insets: linear relations of DPV peak currents for 1′-5 mL-2h/GCE ECS with increasing DOP and AAP concentration, respectively. (b) DPV peak currents for 1′-5 mL/GCE ECS in 0.10 M PBS toward 90 μM DOP and 90 μM AAP in the presence of other different interferences (90 μM) (e.g., pro, ala, cys, arg).

technique in 0.1 M PBS at pH = 7.0. First, the influences of scan rate on the peak currents of DOP for 1′-5 mL-2h/GCE ECS were studied in the existence of 0.50 mM DOP. Upon augmenting the scan rate from 20 to 200 mV s^{-1}, the anodic and cathodic peak currents of DOP increase (Figure S13a, b) and are linearly proportional to the scan rate, which can be separately fitted by I (μA) = 0.16742C (μM) + 8.36733 (R^2 = 0.991) and I (μA) = 0.06846C (μM) + 0.33673 (R^2 = 0.997). Then, the influences of scan rate on the peak currents of AAP for 1′-5 mL-2h/GCE ECS were measured under the same conditions (Figure S13c, d), and the relations of anodic and cathodic peak currents of APP with scan rate can respectively abide by I (μA) = 0.10892C (μM) + 9.12373 (R^2 = 0.983) and I (μA) = 0.05119C (μM) − 3.66767 (R^2 = 0.973). The influences of scan rate on DOP and AAP peak currents in the simultaneous presence of them were also examined (Figure 9). Not surprisingly, the simultaneous testing results of DOP and AAP are consistent with the linearity of separate test results of DOP or AAP, which demonstrates a surface-controlled electrode process.[33,34]

Eventually, the selectivity for 1′-5 mL-2h/GCE ECS toward detecting small biomolecules was investigated under optimum conditions with 90 μM DOP and 90 μM AAP at pH = 7.0. The antijamming capability studies for 1′-5 mL-2h/GCE ECS were performed by DPV measurements (Figure 8b and Figure S14). It can be observed that no remarkable changes in current

https://dx.doi.org/10.1021/acs.inorgchem.0c03556
Inorg. Chem. 2021, 60, 2663−2671

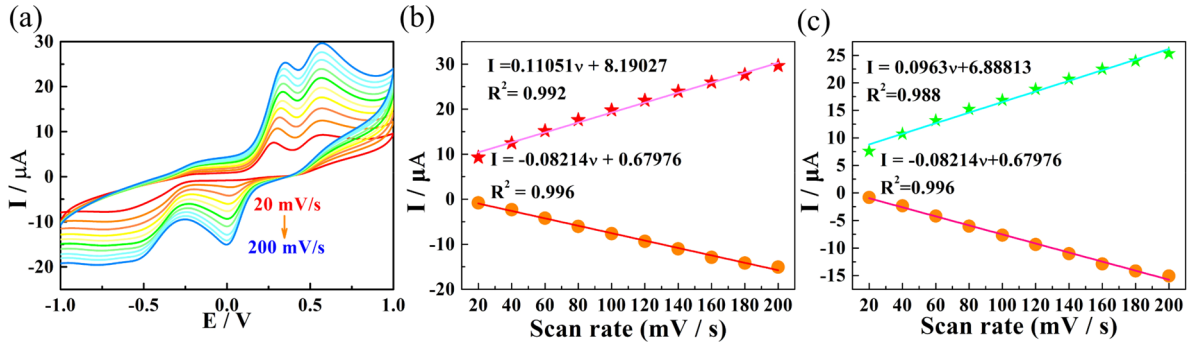

Figure 9. (a) CVs of **1′**-5 mL-2h/GCE ECS at different scan rates (from 20 to 200 mV/s) in the presence of 0.50 mM DOP and 0.50 mM AAP. (b) Relationship of anodic and cathodic peak currents of DOP with the variation of scan rate. (c) Relationship of anodic and cathodic peak currents of AAP with the variation of scan rate.

intensities and potential positions are observed after other 90 μM interfering biological small molecules were added separately into 50 mL of PBS containing 90 μM DOP and 90 μM AAP, including arginine (arg), alanine (ala), proline (pro), and cysteine (cys). The results indicate that **1′**-5 mL-2h/GCE ECS exhibits an excellent antiinterference ability.

CONCLUSIONS

In summary, an unprecedented 3-D TMLnHIOHAT **1** was hydrothermally synthesized. Additionally, uniform cuboid nanocrystal **1′** based on the electrostatic interaction between **1** and K^+ was also successfully fabricated. It was found that the concentration of **1** and K^+ played an important role in the synthesis of nanocrystals of **1′**. Importantly, **1′**-5 mL-2h can work as an electrode modified material, and it was used to construct **1′**-5 mL-2h/GCE ECS, which reveals high sensitivity and selectivity for simultaneous detection of DOP and AAP with a low LOD and good linearity. Furthermore, this work can provide a simple and easy-to-operate example for the preparation of much more novel organic−inorganic hybrid POT-based materials for detecting biological small molecules.

ASSOCIATED CONTENT

Supporting Information

The Supporting Information is available free of charge at https://pubs.acs.org/doi/10.1021/acs.inorgchem.0c03556.

Related structural figures; IR spectra, TG curves, PXRD SEM images, and electrochemical curves (PDF)

Accession Codes

CCDC 2042860 contains the supplementary crystallographic data for this paper. These data can be obtained free of charge via www.ccdc.cam.ac.uk/data_request/cif, or by emailing data_request@ccdc.cam.ac.uk, or by contacting The Cambridge Crystallographic Data Centre, 12 Union Road, Cambridge CB2 1EZ, UK; fax: +44 1223 336033.

AUTHOR INFORMATION

Corresponding Authors

Yanzhou Li − *Henan Key Laboratory of Polyoxometalate Chemistry, College of Chemistry and Chemical Engineering, Henan University, Kaifeng, Henan 475004, People's Republic of China*; Email: liyanzhou@henu.edu.cn

Lijuan Chen − *Henan Key Laboratory of Polyoxometalate Chemistry, College of Chemistry and Chemical Engineering, Henan University, Kaifeng, Henan 475004, People's Republic of China*; Email: ljchen@henu.edu.cn

Junwei Zhao − *Henan Key Laboratory of Polyoxometalate Chemistry, College of Chemistry and Chemical Engineering, Henan University, Kaifeng, Henan 475004, People's Republic of China*; orcid.org/0000-0002-7685-1309; Email: zhaojunwei@henu.edu.cn

Authors

Baoxing Zeng − *Henan Key Laboratory of Polyoxometalate Chemistry, College of Chemistry and Chemical Engineering, Henan University, Kaifeng, Henan 475004, People's Republic of China*

Yan Zhang − *Henan Key Laboratory of Polyoxometalate Chemistry, College of Chemistry and Chemical Engineering, Henan University, Kaifeng, Henan 475004, People's Republic of China*

Yanhong Chen − *Henan Key Laboratory of Polyoxometalate Chemistry, College of Chemistry and Chemical Engineering, Henan University, Kaifeng, Henan 475004, People's Republic of China*

Guoping Liu − *Henan Key Laboratory of Polyoxometalate Chemistry, College of Chemistry and Chemical Engineering, Henan University, Kaifeng, Henan 475004, People's Republic of China*

Complete contact information is available at: https://pubs.acs.org/10.1021/acs.inorgchem.0c03556

Notes

The authors declare no competing financial interest.

ACKNOWLEDGMENTS

This work was supported by the National Natural Science Foundation of China (21871077, 21671054, 21771052, 22001042, 22001058), the Program for Innovation Teams in Science and Technology in Universities of Henan Province (20IRTSTHN004), and the Program of First-Class Discipline Cultivation Project of Henan University (2019YLZDYJ02, CJ1205A0240019).

REFERENCES

(1) Anyushin, A. V.; Kondinski, A.; Parac-Vogt, T. N. Hybrid polyoxometalates as post-functionalization platforms: from fundamentals to emerging applications. *Chem. Soc. Rev.* **2020**, *49*, 382−432.

(2) Zheng, S. T.; Yang, G. Y. Recent advances in paramagnetic-TM-substituted polyoxometalates (TM = Mn, Fe, Co, Ni, Cu). *Chem. Soc. Rev.* **2012**, *41*, 7623−7646.

(3) Li, H. L.; Liu, Y. J.; Liu, J. L.; Chen, L. J.; Zhao, J. W.; Yang, G. Y. Structural transformation from dimerization to tetramerization of

serine-decorated rare-earth-incorporated arsenotungstates induced by the usage of rare-earth salts. *Chem. - Eur. J.* **2017**, *23*, 2673−2689.
(4) Wang, Y. J.; Wu, S. Y.; Sun, Y. Q.; Li, X. X.; Zheng, S. T. Octahedron-shaped three-shell Ln_{14}-substituted polyoxotungstogermanates encapsulating a W_4O_{15} cluster: luminescence and frequency dependent magnetic properties. *Chem. Commun.* **2019**, *55*, 2857−2860.
(5) Lu, B. B.; Yang, J.; Che, G. B.; Pei, W. Y.; Ma, J. F. Organic framework assembled with resorcin[4]arene and polyoxometalate for efficient heterogeneous catalysis of azide−alkyne "click" reaction. *ACS Appl. Mater. Interfaces* **2018**, *10*, 2628−2636.
(6) Han, Z. G.; Zhang, H. X.; Zhang, D. S.; Liu, C. N.; Zheng, R.; Xia, G. B.; Wang, X. X. Sandwich-type polyoxotungstate consisting of two different trilacunary Keggin-type units. *Inorg. Chem.* **2016**, *55*, 12488−12491.
(7) Hu, J. F.; Han, T.; Chi, Y. N.; Lin, Z. G.; Xu, Y. Q.; Yang, S.; Wei, D.; Zheng, Y. Z.; Hu, C. W. Sulfur-centred polyoxoniobate-based 3D organic-inorganic hybrid compound and its magnetic behavior. *Chem. Commun.* **2016**, *52*, 10846−10849.
(8) Ikeda, T.; Hiyoshi, N.; Matsuura, S.; Kodaira, T.; Nakaoka, T.; Irisa, A.; Kawano, M.; Yamamoto, K. Amphiphilic organic-inorganic hybrid zeotype aluminosilicate like a nanoporous crystallized Langmuir-Blodgett film. *Angew. Chem., Int. Ed.* **2015**, *54*, 7994−7998.
(9) Ma, F. J.; Liu, S. X.; Sun, C. Y.; Liang, D. D.; Ren, G. J.; Wei, F.; Chen, Y. G.; Su, Z. M. A sodalite-type porous metal-organic framework with polyoxometalate templates: adsorption and decomposition of dimethyl methylphosphonate. *J. Am. Chem. Soc.* **2011**, *133*, 4178−4181.
(10) Ma, P. T.; Hu, F.; Wang, J. P.; Niu, J. Y. Carboxylate covalently modified polyoxometalates: from synthesis, structural diversity to applications. *Coord. Chem. Rev.* **2019**, *378*, 281−309.
(11) Ismail, A. H.; Bassil, B. S.; Yassin, G. H.; Keita, B.; Kortz, U. $\{W_{48}\}$ Ring opening: Fe_{16}-containing, Ln_4-stabilized 49-tungsto-8-phosphate open wheel $[Fe_{16}O_2(OH)_{23}(H_2O)_9(P_8W_{49}O_{189})Ln_4(H_2O)_{20}]^{11-}$. *Chem. - Eur. J.* **2012**, *18*, 6163−6166.
(12) Gu, Y. N.; Chen, Y.; Wu, Y. L.; Zheng, S. T.; Li, X. X. A series of banana-shaped 3d-4f heterometallic cluster substituted polyoxometalates: syntheses, crystal structures, and magnetic properties. *Inorg. Chem.* **2018**, *57*, 2472−2479.
(13) Zhao, J. W.; Li, Y. Z.; Chen, L. J.; Yang, G. Y. Research progress on polyoxometalate-based transition-metal−rare-earth heterometallic derived materials: synthetic strategies, structural overview and functional applications. *Chem. Commun.* **2016**, *52*, 4418−4445.
(14) Yao, Q.; Fang, H.; Deng, K.; Kan, E.; Jena, P. Superhalogens as building blocks of two-dimensional organic-inorganic hybrid perovskites for optoelectronics applications. *Nanoscale* **2016**, *8*, 17836−17842.
(15) Liu, J. C.; Han, Q.; Chen, L. J.; Zhao, J. W. A brief review of the crucial progress on heterometallic polyoxotungstates in the past decade. *CrystEngComm* **2016**, *18*, 842−862.
(16) Artetxe, B.; Reinoso, S.; SanFelices, L.; Lezama, L.; Gutiérrez-Zorrilla, J. M.; Vicent, C.; Haso, F.; Liu, T. B. New perspectives for old clusters: Anderson-Evans anions as building blocks of large polyoxometalate frameworks in a series of heterometallic 3d-4f species. *Chem. - Eur. J.* **2016**, *22*, 4616−4625.
(17) Cai, J.; Zheng, X. Y.; Xie, J.; Yan, Z. H.; Kong, X. J.; Ren, Y. P.; Long, L. S.; Zheng, L. S. Anion-dependent assembly of heterometallic 3d-4f clusters based on a lacunary polyoxometalate. *Inorg. Chem.* **2017**, *56*, 8439−8445.
(18) Zhao, J. W.; Cao, J.; Li, Y. Z.; Zhang, J.; Chen, L. J. First tungstoantimonate-based transition-metal−lanthanide heterometalic hybrids functionalized by amino acid ligands. *Cryst. Growth Des.* **2014**, *14*, 6217−6229.
(19) Chen, Y. H.; Sun, L. H.; Chang, S. Z.; Chen, L. J.; Zhao, J. W. Synergistic effect between different coordination geometries of lanthanides and various coordination modes of 2-picolinic acid ligands tuning three types of rare 3d-4f heterometallic tungstoantimonates. *Inorg. Chem.* **2018**, *57*, 15079−15092.
(20) Jiang, J.; Chen, Y. H.; Liu, L. L.; Chen, L. J.; Zhao, J. W. 2-Picolinate-decorated iron−lanthanide heterometallic germanotungstates including an S-shaped $[Ge_2W_{20}O_{72}]^{16-}$ segment. *Inorg. Chem.* **2019**, *58*, 15853−15863.
(21) Jordan, J. W.; Lowe, G. A.; McSweeney, R. L.; Stoppiello, C. T.; Lodge, R. W.; Skowron, S. T.; Biskupek, J.; Rance, G. A.; Kaiser, U.; Walsh, D. A.; Newton, G. N.; Khlobystov, A. N. Host-guest hybrid redox materials self-assembled from polyoxometalates and single-walled carbon nanotubes. *Adv. Mater.* **2019**, *31*, 1904182.
(22) Li, X.; Xue, H.; Pang, H. Facile synthesis and shape evolution of well-defined phosphotungstic acid potassium nanocrystals as a highly efficient visible-light-driven photocatalyst. *Nanoscale* **2017**, *9*, 216−222.
(23) Ogasawara, Y.; Uchida, S.; Maruichi, T.; Ishikawa, R.; Shibata, N.; Ikuhara, Y.; Mizuno, N. Cubic cesium hydrogen silicododecatungstate with anisotropic morphology and polyoxometalate vacancies exhibiting selective water sorption and cation-exchange properties. *Chem. Mater.* **2013**, *25*, 905−911.
(24) Wang, H. B.; Yan, Y.; Li, B.; Bi, L. H.; Wu, L. X. Hierarchical self-assembly of surfactant-encapsulated and organically grafted polyoxometalate complexes. *Chem. - Eur. J.* **2011**, *17*, 4273−4282.
(25) Yan, Y.; Li, B.; Li, W.; Li, H.; Wu, L. Controllable vesicular structure and reversal of a surfactant-encapsulated polyoxometalate complex. *Soft Matter* **2009**, *5*, 4047−4053.
(26) Zhou, W. Z.; Feng, X. J.; Tan, H. Q.; Shi, H. F.; Wang, Y. H.; Gao, S.; Li, Y. G. A Surfactant-encapsulating polyoxometalate nanowire assembly as a new carrier for nanoscale noble-metal catalysts. *Chem. - Asian J.* **2016**, *11*, 3107−3112.
(27) Fang, X.; Ren, H.; Zhao, H.; Li, Z. Ultrasensitive visual and colorimetric determination of dopamine based on the prevention of etching of silver nanoprisms by chloride. *Microchim. Acta* **2017**, *184*, 415−421.
(28) Jiang, J.; Du, X. Sensitive electrochemical sensors for simultaneous determination of ascorbic acid, dopamine, and uric acid based on Au@Pd-reduced graphene oxide nanocomposites. *Nanoscale* **2014**, *6*, 11303−11309.
(29) Liu, X.; Zhang, W.; Huang, L.; Hu, N.; Liu, W.; Liu, Y.; Li, S.; Yang, C.; Suo, Y.; Wang, J. Fluorometric determination of dopamine by using molybdenum disulfide quantum dots. *Microchim. Acta* **2018**, *185*, 185.
(30) Zaidi, S. A. Development of molecular imprinted polymers based strategies for the determination of dopamine. *Sens. Actuators, B* **2018**, *265*, 488−497.
(31) Kim, D.; Kim, J. M.; Jeon, Y.; Lee, J.; Oh, J.; Hooch Antink, W.; Kim, D.; Piao, Y. Novel two-step activation of biomass-derived carbon for highly sensitive electrochemical determination of acetaminophen. *Sens. Actuators, B* **2018**, *259*, 50−58.
(32) Adhikari, B. R.; Govindhan, M.; Chen, A. Sensitive detection of acetaminophen with graphene-based electrochemical sensor. *Electrochim. Acta* **2015**, *162*, 198−204.
(33) Alam, A. U.; Qin, Y.; Howlader, M. M.R.; Hu, N.-X.; Deen, M. J. Electrochemical sensing of acetaminophen using multi-walled carbon nanotube and β-cyclodextrin. *Sens. Actuators, B* **2018**, *254*, 896−909.
(34) Alam, A. U.; Qin, Y. H.; Catalano, M.; Wang, L. H.; Kim, M. J.; Howlader, M. M. R.; Hu, N. X.; Deen, M. J. Tailoring MWCNTs and β-cyclodextrin for sensitive detection of acetaminophen and estrogen. *ACS Appl. Mater. Interfaces* **2018**, *10*, 21411−21427.

https://dx.doi.org/10.1021/acs.inorgchem.0c03556
Inorg. Chem. 2021, 60, 2663−2671